Journal of Materials Chemistry A

Impact of trace extrinsic defect formation on the local symmetry transition in spinel $LiNi_{0.5}Mn_{1.5}O_{4-\delta}$ and their electrochemical characteristics

Journal:	*Journal of Materials Chemistry A*
Manuscript ID	TA-ART-08-2018-007825.R1
Article Type:	Paper
Date Submitted by the Author:	07-Oct-2018
Complete List of Authors:	Shiiba, Hiromasa; Shinshu University, Department of Materials Chemistry Zettsu, Nobuyuki; Shinshu University, Center for Energy & Environmental Science; Shinshu University, Department of Materials Chemistry Kida, Satoru; Shinshu University, Department of Materials Chemistry Kim, Dae-wook; Shinshu University, Department of Materials Chemistry Teshima, Katsuya; Shinshu University, Center for Energy & Environmental Science; Shinshu University, Department of Materials Chemistry

Journal Name

ARTICLE

Impact of trace extrinsic defect formation on the local symmetry transition in spinel $LiNi_{0.5}Mn_{1.5}O_{4-\delta}$ and their electrochemical characteristics

Received 00th January 20xx,
Accepted 00th January 20xx

DOI: 10.1039/x0xx00000x

www.rsc.org/

Hiromasa Shiiba,[a,‡] Nobuyuki Zettsu,[a,b,‡,*] Satoru Kida,[a] Dae-wook Kim[a], and Katsuya Teshima[a,b,*]

Many fundamental studies have been conducted on the electrochemical and electronic structures in transition metal cation-substituted $LiNi_{0.5}Mn_{1.5}O_4$ systems. These systems have potential use as 5V-level high voltage cathode materials for lithium ion batteries, but there are only a few reports regarding the control of their symmetry transitions which contribute the electronic structures and Li^+ transport efficiency. We address this solid chemistry and the corresponding electrochemical characteristics using both systematic experimental and theoretical approaches. Trace substitution of Cu^{2+} with Mn^{4+} (Cu_{Mn}) can promote the symmetry transition from *Fd*-3*m* to $P4_332$ phase in oxygen-deficient $LiNi_{0.5}Mn_{1.5}O_{4-\delta}$. This behavior is detectable by Fourier-transform infrared and Raman spectroscopies but undetectable by X-ray diffraction, suggesting that the symmetry transition was localized in the space near the point of extrinsic defects Cu_{Mn} in the spinel framework. Notably, a very small amount of Cu^{2+} substitution not only affects the local atomic arrangement but also remarkably affects the macroscopic electrochemical redox responsiveness, including the inactivation of Mn^{3+}/Mn^{4+} redox couples, suppression of Mn ion dissolution, and enhancing the c rate capability (increasing the electron conductivity, and reducing the activation barrier for lithium ion hopping along the most energetically preferable 8*a*–16*c*–8*a* route) and cyclability.

Introduction

Current development of lithium ion secondary battery (LIB) technologies has been the driving force behind the move towards digital technology-driven lifestyles in recent years[1]. However, their technical requirements are undergoing major changes with respect to energy density, and require higher-energy-density cathode materials[2]. The cathode's energy density depends on the specific capacity, tap density, loading amount, and average operating voltage of the active materials. High-voltage materials can reduce the number of serially connected cells and enhance the energy density of the system. For instance, cubic $LiNi_{0.5}Mn_{1.5}O_4$ with a spinel framework has a higher gravimetric energy density of 686 W·h·kg^{-1}, compared to other candidate cathode materials including $LiCoO_2$ (518 W·h·kg^{-1}), $LiNiO_2$ (630 W·h·kg^{-1}), $LiMn_2O_4$ (440 W·h·kg^{-1}), $LiFePO_4$ (495 W·h·kg^{-1}), Li_2FePO_4F (414 W·h·kg^{-1}), and $Li(Ni_{1/3}Mn_{1/3}Co_{1/3})O_2$ (576 W·h·kg^{-1})[3]. In recent years, studies on $LiNi_{0.5}Mn_{1.5}O_4$ have focused primarily on improving its electrochemical performance using various methods, such as transition metal cation substitution of Mg, Ti, V, Cr, Fe, Co, Al, Cu, Zn, Sn, Ru, Rh, and Sm with Ni^{2+} or Mn^{4+} and F^- passivation with oxygen-deficient materials, or surface modification with ZnO, Al_2O_3, Bi_2O_3, $BaTiO_3$, and fluoroalkylsilane self-assembled monolayers (SAM)[4-23].

Many fundamental studies have been conducted on the electrochemical and electronic structures of 5V-level high voltage cathode materials for use in LIBs, but there are only a few reports on controlling their local symmetry transitions, accompanied by Li^+ hopping behavior[9]. Cubic $LiNi_{0.5}Mn_{1.5}O_4$ is well known as a solid solution composed of layered $LiNiO_2$ and spinel $LiMn_2O_4$, which has a spinel framework with two different space groups of ordered $P4_332$ and disordered *Fd*-3*m*, respectively, depending on the atomic arrangement of Ni^{2+}/Mn^{4+}[24, 25]. Ni and Mn ions occupy Wyckoff positions at 4b and 12d sites in $P4_332$, whereas they randomly occupy crystallographically-equivalent 16d sites in *Fd*-3*m*. In addition, disordered *Fd*-3*m* is prone to contain oxygen deficiencies, described as $LiNi_{0.5}Mn_{1.5}O_{4-\delta}$, accompanying the reduction of Mn ion from Mn^{4+} to Mn^{3+}. Synthesis of pure $P4_332$ symmetry is difficult to achieve because oxygen deficiency naturally occurs when calcining at > 600°C. Mn^{3+} is then produced due to charge neutralization, resulting in a phase transition from $P4_332$ to *Fd*-3*m*. According to previous studies, this material's electrochemical properties are sensitive to synthesis

[a] Department of Materials Chemistry, Faculty of Engineering, Shinshu University, 4-17-1 Wakasato, Nagano 380-8553, Japan.
[b] Center for Energy and Environmental Science, Shinshu University, 4-17-1 Wakasato, Nagano 380-8553, Japan.
‡ These authors contributed equally.
Electronic Supplementary Information (ESI) available: Figures of details on the data necessary to derive the calculation result on the defect formation energies, Rietveld refinement results of the Cu-incorporated LNMO, theoretical voltage profile, atomic valence distributions of Cu-incorporated LNMO. Table of chemical composition of Cu-incorporated LNMO by ICP-OES. See DOI: 10.1039/x0xx00000x

conditions, and it is prone to capacity fading[24, 25]. Additionally, there is ample evidence that ordering between the Mn^{4+} and Ni^{2+} ions decrease the electronic conductivity and increases internal resistance because of active $Ni^{2+}/^{3+}/^{4+}$ multiple redox centers isolated amidst inactive Mn^{4+} ions[26-34]. One widely-accepted strategy to combat this issue has been to partially substitute other metal ions for Ni^{2+}, which disrupts cation ordering and stabilizes the cycling performance. For instance, Zhu *et al.* reported that substituted Co and Cu randomly occupy the octahedral 16d sites, enhancing the electronic conductivity by promoting disorder[4]. Yang *et al.* analyzed the Li diffusion activation barriers of $LiM_{0.5-x}Mn_{1.5}M_xO_4$ (M = Ti, V, Cr, Fe, Co, Ni, and Cu) using *ab initio* density functional theory (DFT) calculations[9]. Extrinsic defect formation due to dopants highly affects the Li^+ diffusion barriers. In particular, $LiCu_{0.25}Ni_{0.25}Mn_{1.5}O_4$ exhibited higher capacity than $LiM_{0.5}Mn_{1.5}O_4$ under cycling with high current density. This could be attributed to the single-phase reaction during charging, the lower Li diffusion barrier, and the higher electronic conductivity.

The origin of the symmetry transition and corresponding enhanced electrochemical performance are not fully understood in relation to the electrical and structural properties of these materials, which are in turn affected by the electronic and ionic conductivities. Here, we address this solid chemistry and its corresponding electrochemical characteristics using both systematic experimental and theoretical approaches. A trace amount substitution of Cu^{2+} with Mn^{4+} (Cu_{Mn}) can promote the symmetry transition from *Fd*-3*m* to $P4_332$ in oxygen-deficient $LiNi_{0.5}Mn_{1.5}O_{4-\delta}$ systems.

Experimental section

***Ab initio* DFT calculations.** The Vienna *ab initio* simulation package[35, 36] was used with the generalized gradient approximation (GGA-PBEsol) + *U*[37] and projector-augmented wave methods[38]. For the GGA + *U* calculations, the *U* values for the *d*-orbitals of Ni and Mn were respectively set to 6.0 and 3.9 eV based on previous reports[39]. An energy cutoff of 500 eV and a *k*-point mesh were chosen so that the product of the number of *k*-points and the number of atoms in the unit cell was greater than 1000. A superstructure of 56 atoms in a cubic spinel lattice of $8LiNi_{0.5}Mn_{1.5}O_4$ was used for all calculations. Relaxation of the crystal structure was allowed for all models, and the final energies of the optimized structural geometries were recalculated to correct for changes in the plane-wave basis during relaxation. Naturally, Ni^{2+} and Mn^{4+} completely occupy the crystallographically-equivalent 16d site at random, however we used the most energetically-stable model for calculation in this work. As in our previous study[40], we used the uniform Ni/Mn distribution arrangement for modeling disordered *Fd*-3*m* structures, as originally calculated by Lee and Persson[41, 42]; this is the most stable local cation arrangements as evaluated by Monte Carlo analysis. Nonstoichiometric defect formation energies were calculated by using two different oxygen-deficient models, including an oxygen vacancy model and a metal-excess model. Since an extinct transition metal cation of M was incorporated in the neighboring oxygen vacancy site in the oxygen vacancy model, three possible sites exist in $P4_332$: i) M_{Ni} with oxygen vacancies at neighboring 24e sites (each oxygen vacancy is surrounded by two Mn and one M_{Ni}), ii) M_{Mn} with oxygen vacancies at neighboring 24e sites (each oxygen vacancy is surrounded by one Ni, one Mn and one M_{Mn}), iii) M_{Mn} with oxygen vacancies at neighboring 8c sites (each oxygen vacancy is surrounded by two Mn and one M_{Mn}). In contrast, three different possible sites exist for *Fd*-3*m* type symmetry: i) M_{Ni} with oxygen vacancies at neighboring O@Ni1Mn2 sites (each oxygen vacancy is surrounded by two Mn and one M_{Ni}), ii) M_{Mn} with oxygen vacancies at neighboring O@Ni1Mn2 sites (each oxygen vacancy is surrounded by one Ni, one Mn and one M_{Mn}), iii) M_{Mn} with oxygen vacancies at neighboring O@Mn3 sites (each oxygen vacancy is surrounded by two Mn and one M_{Mn}). The defect formation energies for the metal-excess model in $P4_332$ and *Fd*-3*m* $LiNi_{0.5-x}Mn_{1.5}M_xO_4$ and $LiNi_{0.5}Mn_{1.5-y}M_yO_4$ ($0 \le x \le 0.125$, $0 \le y \le 0.125$) were calculated as

$$E^F = \frac{1}{4}\left\{\begin{array}{c} E(Li_9Ni_4Mn_{12}O_{32}) \\ +\left(\frac{1}{2}-25x\right)E(Li_8Ni_5Mn_{12}O_{32}) \\ +\frac{3}{2}E(Li_8Ni_4Mn_{13}O_{32}) \\ +25xE(Li_8Ni_4Mn_{12}M_1O_{32}) \\ -25xE(Li_8Ni_3Mn_{12}M_1O_{32}) \\ -(25-200x)E(LiNi_{0.5}Mn_{1.5}O_4) \end{array}\right\} + \frac{1}{2}E(O_2) \quad (1)$$

$$E^F = \frac{1}{4}\left\{\begin{array}{c} E(Li_9Ni_4Mn_{12}O_{32}) \\ +\frac{1}{2}E(Li_8Ni_5Mn_{12}O_{32}) \\ +\left(\frac{3}{2}-25y\right)E(Li_8Ni_4Mn_{13}O_{32}) \\ +25yE(Li_8Ni_4Mn_{12}M_1O_{32}) \\ -25yE(Li_8Ni_4Mn_{11}M_1O_{32}) \\ -(25-200y)E(LiNi_{0.5}Mn_{1.5}O_4) \end{array}\right\} + \frac{1}{2}E(O_2) \quad (2)$$

The energy correction for O_2 molecules was used for all calculations as reported by Wang *et al*[43].

Flux growth of $LiNi_{0.5}Mn_{1.5}O_{4-\delta}$ and related compounds single crystals. The flux growth of $LiNi_{0.5}Mn_{1.5}O_{4-\delta}$ crystals was obtained from a stoichiometric mixture of $Ni(NO_3)_2$, $Mn(NO_3)_2$ and LiCl and using a binary flux of LiCl and KCl. We further added 1 mol% of $Cu(NO_3)_2$ as a copper source into the above flux growth system for Cu incorporation. All chemicals were purchased from Wako Pure Chemical Industries, Ltd. and were used without any additional purification. All powders were mixed in an alumina crucible (30 mL volume). The solute concentration was controlled to be approximately 8 mol% for the flux growth reactions. The mixture was then heated to 700 °C in an electric furnace at a rate of 900 °C·h^{-1}. After maintaining this temperature for 10 h, the crucible was cooled to 500 °C at a rate of 200 °C·h^{-1}. The heated powders were then allowed to naturally cool to room temperature in the furnace. The powders were washed with warm water to remove the remaining flux. Finally, the powders were annealed under an O_2 atmosphere at 700 °C for 10 h.

Preparation and characterization of SAM-coated electrodes. SAM was formed on the surface of Cu-substituted $LNMO_{4-\delta}$ crystals via the vapor phase deposition conducted at a temperature of 150 °C and atmospheric pressure.[22,23] Fluoroalkylsilane (FAS17: $F_3C(CF_2)_7(CH_2)_3Si(OCH_3)_3$ was used as precursor molecules for SAM coatings. Although liquid-phase processing is typically used for SAM preparation, the specified vapor-phase process was utilized in this study because it was expected to reduce the deposition of aggregated FAS17 molecules, which tended to degrade the quality of the produced SAMs.

Characterization. The phases and structures of the crystals were identified using X-ray diffraction (XRD) with a Cu-Kα radiation source. The X-ray diffractometer (Miniflex II, Rigaku) was operated at 30 kV and 20 mA, with 2θ = 10–80° (scan step = 0.02°). Field emission scanning electron microscopy (FE-SEM; JSM-7600F at 15 kV; JEOL, Japan) observations were conducted to examine the microstructures in the crystals. The valence state of the Mn ion and atomic percentage of incorporated fluorine atoms were studied by X-ray photoelectron spectroscopy (XPS) with a monochromic Al-Kα source (JPS-9010MX at 15 kV, 15 mA; JEOL). All binding energies in the spectra were referenced to the C1s hydrocarbon peak at 284.5 eV. The orders of the Ni and Mn configurations were characterized by Raman spectroscopy with 532 nm excitation (LabRAM, Horiba, Japan), and Fourier-transform infrared (FT-IR) spectroscopy (FT-IR 4600, JASCO, Japan). The electrochemical characteristics were evaluated using a coin-type cell (R2032). The cathode was prepared by a conventional pasting process and contained spinel crystals, acetylene black and polyvinylidene fluoride (90:5:5 wt%). The mixture was diluted with *N*-methyl-2-pyrrolidone to a viscosity of ~5.1 Pa·s. The prepared paste was homogeneously coated onto a 20-µm-thick Al foil using a slit coater. The electrode density was adjusted to 3.0 g·cm^{-3} using a press machine. All electrodes were dried at 120 °C in a vacuum oven prior to cell assembly. Lithium metal foil and a porous polypropylene film (Celgard #2500) were used as the counter electrode and separator, respectively. A solution of 1 M $LiPF_6$ in a mixture of ethylene carbonate and dimethyl carbonate (1:1 v/v) was used as the electrolyte. The coin-type cells were assembled in an Ar-filled glovebox (MDB-2BL, Miwa Mfg Co., Ltd., Japan) with a controlled atmosphere containing < 1 ppm H_2O and O_2. Galvanostatic charge–discharge tests were performed using a potentio/galvanostat (HJ1020Msd8, Hokuto Denko, Japan). The cut-off voltage range for the battery tests was controlled between 3.5 and 4.8 V vs. Li/Li$^+$.

Results and discussion

We investigated the phase stabilities for both oxygen-deficient $LiNi_{0.5-x}Mn_{1.5}M_xO_{4-\delta}$ and $LiNi_{0.5}Mn_{1.5-y}M_yO_{4-\delta}$ ($0 \le x \le 0.125$, $0 \le y \le 0.125$, M = Ti, V, Cr, Fe, Co, Cu, Zn, Sn, $0 \le x \le 0.125$, $0 \le y \le 0.125$) with different symmetries of $P4_332$ and *Fd*-3*m*. The defect formation difference in ($E^F(Fd\text{-}3m) - E^F(P4_332)$) between the oxygen vacancy model and metal-excess model is summarized in Figure 1. Details on the data necessary to derive the calculation result on the defect formation energies

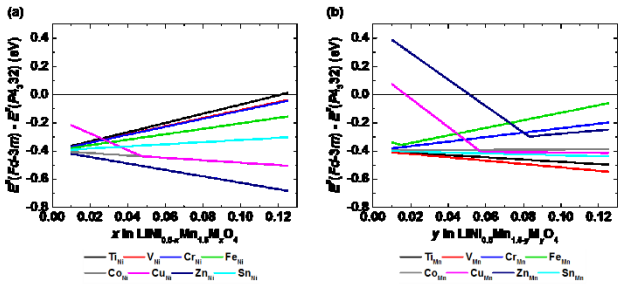

Figure 1. Differences in the defect formation energies between $P4_332$ and *Fd*-3*m* type symmetries in both the oxygen vacancy model and metal-excess model for (a) $LiNi_{0.5-x}Mn_{1.5}M_xO_4$ and (b) $LiNi_{0.5}Mn_{1.5-y}M_yO_4$ ($0 \le x \le 0.125$, $0 \le y \le 0.125$).

are described in Supplementary Figures S2–S5. The symmetry transition from $P4_332$ to *Fd*-3*m* in the spinel system was significantly influenced by both substituted transition metal species and the amounts of substitution. Positive values in the y-axis indicate that the substituted metal stabilizes the order for $P4_332$ symmetry even if oxygen deficiencies are present in the framework. Furthermore, we found two different trends associated with the incorporated amounts. Minimal substitution of Cu^{2+} and Zn^{2+} with Mn^{4+} (Cu_{Mn}, Zn_{Mn}) stabilized the $P4_332$ phase, but their formation energies became more unstable when increasing the substitution amount. In contrast, the $P4_332$ symmetry was stabilized under relatively higher substitution amounts for Ti^{4+} and V^{4+} in Ni^{2+} sites (Ti_{Ni}, V_{Ni},).

To understand these opposing trends, we further evaluated anti-site defects formation energies, oxygen vacancy formation energies, and defect formation energies in both $P4_332$ and *Fd*-3*m* type $LiNi_{0.5-x}Mn_{1.5}M_xO_4$ and $LiNi_{0.5}Mn_{1.5-y}M_yO_4$ ($0 \le x \le 0.125$, $0 \le y \le 0.125$), respectively. Valence states of all aliovalent transition metals were stabilized to Ti^{4+}, V^{4+}, Cr^{3+}, Fe^{3+}, Co^{2+}, Cu^{2+}, Zn^{2+}, Sn^{4+} during relaxation in the calculation, which are independent of the native transition metals in $LiNi_{0.5}Mn_{1.5}O_4$ according to the calculation results (Supplementary Figure 2). In addition, a series of extrinsic defects, represented as Ti_{Ni}, V_{Ni}, Cr_{Ni}, Fe_{Ni}, Sn_{Ni}, Cu_{Mn}, and Zn_{Mn} reduced Mn^{4+} to Mn^{3+} due to charge balancing in the lattice. These results on both oxygen vacancy formation energies for oxygen vacancy models and defect formation energies for metal-excess model strongly suggest that both $Cu^{2+}_{0.01}$ and $Zn^{2+}_{0.01}$ substitution with $Mn^{4+}_{0.01}$ are the most promising candidates for stabilization of $P4_332$-type cation arrangements in spinel frameworks, associated with ease of O_2 release from the lattice. In contrast, all other candidates preferentially formed interstitial solid solutions in which these other transition metals occupied the interstitial 4a sites, associated with Mn^{4+} occupying 12d sites being reduced to Mn^{3+} to neutralize the generated effective charges. Charge neutralization promoted the anti-site defect formation, accelerating the symmetry transition to the *Fd*-3*m* phase.

Most important pointing out in our computational studies is that the trace substitution of Cu^{2+} or Zn^{2+} with Mn^{4+} (Cu_{Mn}, Zn_{Mn}) provided different oxygen defect formation mechanism contrast to that of other systems. Thus, oxygen vacancy mechanism for $Cu^{2+}_{0.01}$ and $Zn^{2+}_{0.01}$ substitution with $Mn^{4+}_{0.01}$ exceptionally prevent the formation of Mn^{3+}, even though

metal-excess mechanism for $Cu^{2+}_{0.01}$ and $Zn^{2+}_{0.01}$ substitution with $Mn^{4+}_{0.01}$ form Mn^{3+}.

The cases of high amounts of substitution exhibited different trends. The formation energy in the $P4_332$ type spinel framework stabilized with Cu^{2+} and Zn^{2+} also increased positively as the amount of substitution increased. The symmetry of Ni/Mn arrangements transitioned completely to the *Fd*-3*m* phase in association with interstitial solid solution formation. Excess transition metal cations preferentially occupied interstitial 4a sites, triggering the *Fd*-3*m* phase transition. We speculate that the threshold for the symmetry transition can be explained in terms of limitations in allowable lattice volume. The lattice volume of the stoichiometric *Fd*-3*m* type $LiNi_{0.5}Mn_{1.5}O_4$ (8.172Å) is larger than that of $P4_332$ type (8.166Å)[25]. Therefore, transition metal ions with smaller ionic radii can penetrate into interstitial vacancy sites and expand the lattice volume, leading to the formation of *Fd*-3*m* type symmetry. In contrast, the Ti^{4+} occupying Ni^{2+} 4b sites created different characteristics in the defect formation energy compared to the substitution amount. The energies became smaller as the amount of substitution increased. Even though the substituted Ti^{4+} increases the presence of Mn^{3+}, the oxygen deficient $LiNi_{0.5-x}Mn_{1.5}Ti_xO_{4-\delta}$ ($x \geq 0.12$) has the potential to form $P4_332$ symmetry. Their atomic arrangement based on DFT calculations suggests that the aliovalent Ti^{4+} preferentially occupied Mn^{4+} 12d sites in the spinel lattice, reducing Mn^{4+} to Mn^{3+} and promoting Mn^{3+}/Ti^{4+} anti-site defects.

Figure 2 shows the powder XRD pattern, SEM image and size distribution for the Cu^{2+}-substituted $LiNi_{0.5}Mn_{1.5}O_{4-\delta}$ crystal. All diffraction lines can be assigned to $LiNi_{0.5}Mn_{1.5}O_4$ with *Fd*-3*m* symmetry (ICDD PDF 70-8650). The lattice constant decreased from 8.175 to 8.170 Å due to Cu^{2+} incorporation, close to the experimental value for $P4_332$-type symmetry[25]. FE-SEM revealed octahedral crystals having well-defined facets which were dominantly formed independent of the Cu^{2+} substitution. In contrast to their morphological characteristics, Cu^{2+} substitution decreased the average crystal size (D_{50}) from 1.0 µm to 0.7 µm[22]. Small amounts of Cu^{2+} incorporation can significantly change the size of critical nuclei in the molten LiCl-KCl flux at 700 °C. It promotes greater nuclear formation at the initial stage of crystal growth. The size effects should be contributing the enhancement of electrochemical performance of our cells, especially to the C rate capability) described below in Figure 6a.

Chemical composition analysis based on inductively-coupled plasma optical emission spectrometry (ICP-OES) is summarized in Supplementary Table S1. Rietveld refinement (Supplementary Figure S6a) also suggests that a tiny amount of Cu^{2+} was incorporated in the spinel lattice, represented in the molecular formula as $LiNi_{0.49}Cu_{0.01}Mn_{1.49}O_{3.62}$. The diffraction profile assignable to the $P4_332$ symmetry was not compatible with that of $LiNi_{0.49}Cu_{0.01}Mn_{1.49}O_{3.62}$, suggesting that its average structure as evaluated by XRD can be assigned to spinel structure with *Fd*-3m symmetry. In contrast, the effect of Cu^{2+} on the ordering of the Ni/Mn arrangement was clearly observed using both Raman and FT-IR spectroscopies. These spectra are useful for identifying the local structure more clearly from the viewpoint of vibrational spectroscopy. As shown in Figure 3a, intense and split Raman shifts centered at 498 cm^{-1} and 638 cm^{-1} clearly appeared for $LiNi_{0.49}Cu_{0.01}Mn_{1.49}O_{3.62}$ in contrast to those of broaden peaks in $LiNi_{0.5}Mn_{1.5}O_{4-\delta}$. This discrepancy strongly suggests those compounds have different Ni^{2+}/Mn^{4+} orientation on a Li occupation site basis. Oh et al. and Julien reported that the strong band at 635 cm^{-1} can be assigned to the symmetric Mn-O stretching mode of octahedral MnO_6 (A_{1g}). Both peaks around 402 and 494 cm^{-1} are associated with the Ni^{2+}-O

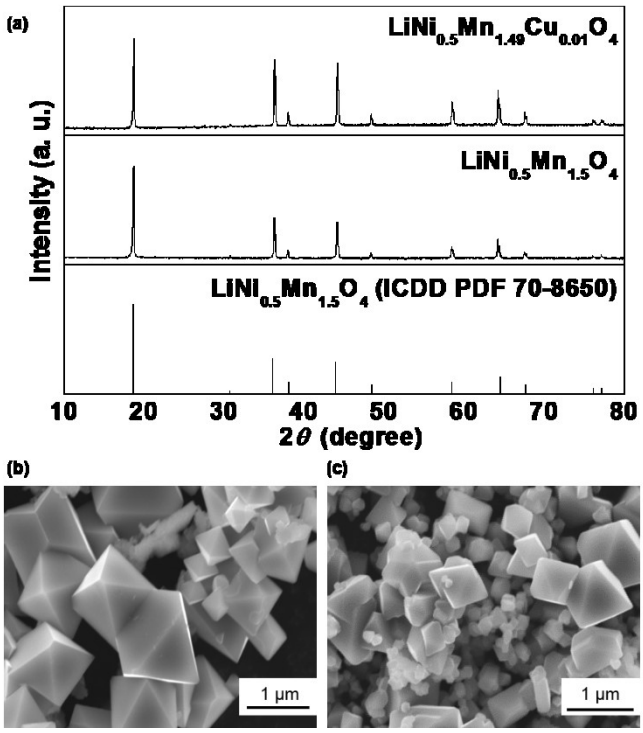

Figure 2. Powder XRD patterns and FE-SEM images of $LiNi_{0.5}Mn_{1.5}O_{4-\delta}$ and $LiNi_{0.5}Mn_{1.49}Cu_{0.01}O_{4-\delta}$ crystals.

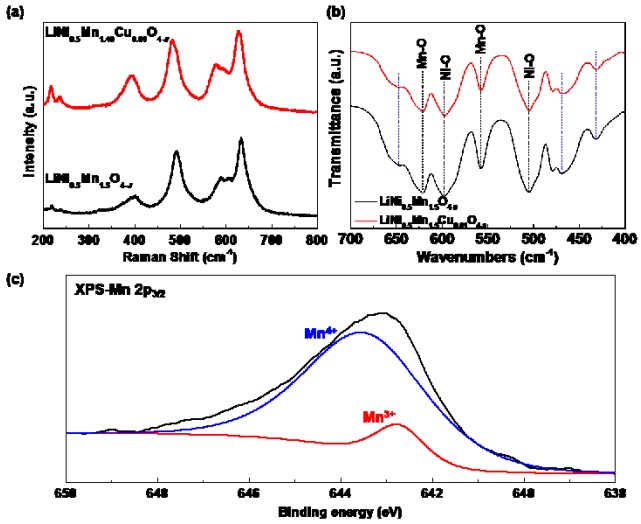

Figure 3. (a) Raman shift, (b) FT-IR and (c) XPS spectra of $LiNi_{0.5}Mn_{1.5}O_{4-\delta}$ and $LiNi_{0.5}Mn_{1.49}Cu_{0.01}O_{4-\delta}$.

stretching mode in the structure[44, 45]. The peak near 580–606 cm^{-1} is considered as T_{2g} for the spinel compounds. The splitting of the T_{2g} band is often considered as obvious evidence of the ordered structure of the spinel. These Raman spectra trends are consistent with FT-IR spectral data. The infrared spectra of $LiNi_{0.49}Cu_{0.01}Mn_{1.49}O_{3.62}$ are shown in Figure 3b, showing eight well-resolved absorption bands. As the $P4_332$ type has eight IR absorption bands while the *Fd*-3*m* type has only five[46], all these results indicate that the arrangement of Ni and Mn ions is promoted locally by minimal Cu^{2+} incorporation. These results suggest that the incorporated Cu^{2+} promotes the local orientation of Ni/Mn arrangement in the spinel lattice. The proportion of Mn^{3+}/Mn^{4+} as determined by XPS (Figure 3c) also strongly supports our theory. Two peaks attributed to Mn^{3+} and Mn^{4+} were observed in the Mn2p core level spectra. The Mn^{4+}/Mn^{3+} ratio for the $LiNi_{0.5}Mn_{1.5}O_{4-\delta}$ crystal was higher than that for $LiNi_{0.49}Cu_{0.01}Mn_{1.49}O_{3.62}$, which agrees with our computational predictions (1.15 for $LiNi_{0.5}Mn_{1.5}O_{4-\delta}$, and 1.36 for $LiNi_{0.5}Cu_{0.1}Mn_{1.49}O_{4-\delta}$).

Galvanostatic charge–discharge tests were performed at a cut-off voltage range of 3.5–4.8 V (vs Li^+/Li). Figure 4(a) shows the third cycled profiles at a current density corresponding to 0.2 C. The maximum discharge capacity was 138 $mAh\cdot g^{-1}$ in the $LiNi_{0.49}Cu_{0.01}Mn_{1.49}O_{3.62}$ electrodes. The coulomb efficiency in the initial cycles of the cell was ca. 0.95% regardless of the Cu^{2+} substitution. Even if the tap density was approximately 3.0 $g\cdot cm^{-3}$, a discharge capacity close to the theoretical capacity

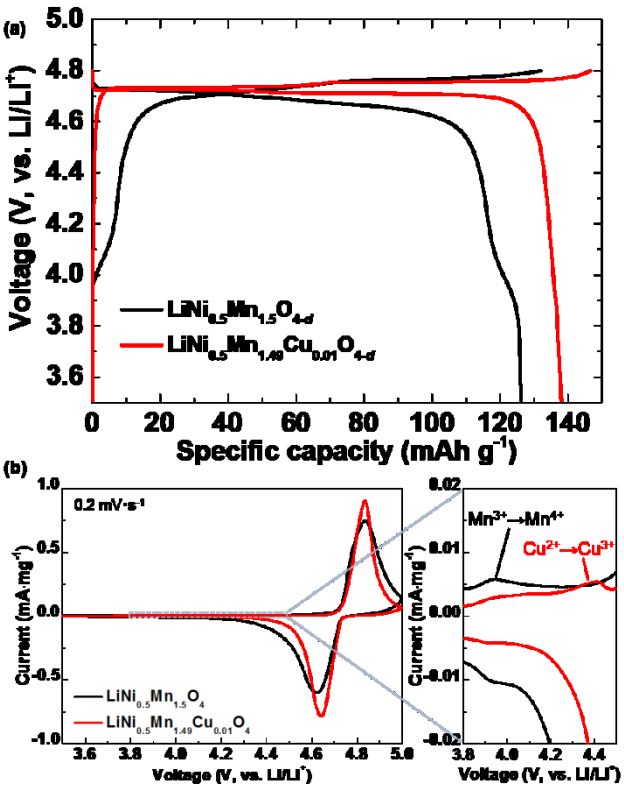

Figure 4. (a) Third cycle charge–discharge profiles at a current density corresponding to 0.2 C at room temperature and (b) cyclic voltammograms of $LiNi_{0.5}Mn_{1.5}O_{4-\delta}$/Li and $LiNi_{0.49}Cu_{0.01}Mn_{1.49}O_{3.62}$/Li cells.

was obtained. Note that Cu^{2+} substitution significantly affected the voltage slope characteristics. Continuous gentle changes of the flat voltage were observed during the discharge reactions from 4.6–4.8 V (vs Li^+/Li), indicating two redox couples (Ni^{2+}/Ni^{3+} and Ni^{3+}/Ni^{4+}). The inflexion point in the voltage slope at ~4.0 V, which was assigned to the redox response from Mn^{3+}/Mn^{4+}, also disappeared. Figure 4(b) shows the cyclic voltammetry of the $LiNi_{0.5}Mn_{1.5}O_{4-\delta}$ and $LiNi_{0.49}Cu_{0.01}Mn_{1.49}O_{3.62}$ crystal electrodes, respectively. Cu^{2+} incorporation made both the oxidation and reduction waves sharper, implying a faster lithiation/delithiation reaction corresponding to the Ni^{2+}/Ni^{3+} and Ni^{3+}/Ni^{4+} redox pairs, which were the origin of the voltage step at the lower Li content region in the voltage profiles. Furthermore, the Mn^{3+}/Mn^{4+} redox peaks obviously faded. Meanwhile, a small peak centered at 4.4 V newly appeared in the oxidation wave of the $LiNi_{0.49}Cu_{0.01}Mn_{1.49}O_{3.62}$ crystal electrodes. We further synthesized another example of the Zn^{2+}-substitution of $LiNi_{0.49}Zn_{0.01}Mn_{1.48}O_{4-\delta}$. As shown in Supplementary Figure S7(a), the third cycled galvanostatic charge-discharge profiles showed continuous gentle changes of the flat voltage during the discharge reactions from 4.6–4.8 V (vs Li^+/Li) as same as that of $LiNi_{0.49}Cu_{0.01}Mn_{1.49}O_{3.62}$. However, the maximum discharge capacity was significantly faded to 102 $mAh\cdot g^{-1}$ in the $LiNi_{0.49}Zn_{0.01}Mn_{1.48}O_{4-\delta}$ electrodes. The Raman shift was also shown in Figure S7(b). Our DFT calculation further implied he anti-cite defect of Li^+/Zn^{2+} was preferentially occurred in $LiNi_{0.5}Mn_{1.375}Zn_{0.125}O_{3.875}$ (see Figure S7(c)). These all electrochemical and structural features has been provided as the supporting experimental evidence, and suggests that the orientation of Ni^{2+} and Mn^{4+} is promoted locally, leading to form $P4_332$ symmetry by minimal Zn^{2+} incorporation.

The changes in the most stable atomic structure as a function of lithium composition in $LiNi_{0.5}Mn_{1.375}Cu_{0.125}O_{3.875}$ were computed using the formation energies of different atomic arrangements to analyze a plausible reaction mechanism for the charge–discharge reaction, based on the voltage slopes. As shown in Supplementary Figure S8(a), delithiation in this system is driven by a solid-solution mechanism ranging from $LiNi_{0.5}Mn_{1.375}Cu_{0.125}O_{3.875}$ to $Li_{0.75}Ni_{0.5}Mn_{1.375}Cu_{0.125}O_{3.875}$. Further delithiation is controlled by a two-phase transition mechanism. The same calculation results can transform to the voltage profile (vs. Li^+/Li). As shown in Supplementary Figure S8(b), the voltage profile at 4.1–4.7 V (associated with the delithiation reaction from $Li_{1.0}$ to $Li_{0.75}$) features two stages,

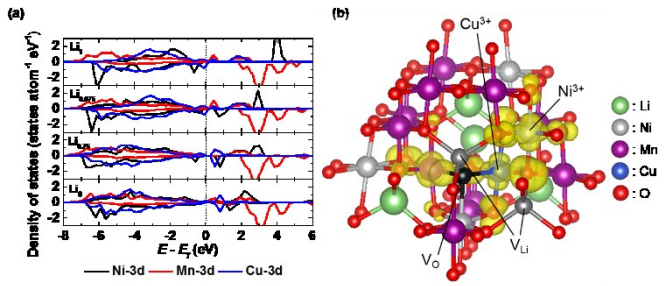

Figure 5. (a) Changes in partial density of states for Ni, Mn and Cu ions during delithiation in $Li_{1-x}Ni_{0.5}Mn_{1.375}Cu_{0.125}O_{3.875}$. (b) Visualization of the hole trajectories generated in the 0–1 eV region at the lower end of the conduction band in $Li_{0.75}Ni_{0.5}Mn_{1.375}Cu_{0.125}O_{3.875}$.

which is consistent with the experimental results. In order to determine which Li^+ occupying the spinel lattice is preferentially delithiated, we performed further DFT calculations on the changes in partial density of states (PDOS) for Ni, Mn and Cu ions (Figure 5(a)) and the visualization of the hole trajectories generated in the 0–1 eV region at the lower end of the conduction band (Figure 5(b)) during delithiation of $LiNi_{0.5}Mn_{1.375}Cu_{0.125}O_{3.875}$. The PDOS profile of Ni-3d drastically changed in the first step, implying that the Li Li^+ were deintercalated in association with the oxidation reaction of Ni^{2+} to Ni^{3+}. In contrast, that of Cu-4d obviously changed in the second step. Subsequent changes were not observed in the PDOS of Cu-4d during further delithiation, which suggests that the Cu^{2+} was fully oxidized to Cu^{3+} at the $Li_{0.75}$ composition. Furthermore, the visualized hole trajectories reveal that Li ions occupying the sites adjacent to oxygen vacancies were preferentially eliminated, relying on the electrochemically active transition metal species at the specified voltage. All results described here suggest that the emerging oxidation-reduction waves in the CV curve can be assigned to the presence of Cu^{2+}/Cu^{3+} redox pairs. Thus, even in the presence of *Fd*-3*m* symmetry and oxygen defects in the spinel lattice, the Cu^{2+}-incorporated spinel derivative with local ordered Ni^{2+}/Mn^{4+} arrangement exhibited electrochemical characteristics similar to the $P4_332$ structure. This is because Cu_{Mn} compensates its charge balance, leading to inhibit Mn^{3+} formation as predicted by our DFT calculation (Supplementary Figure S9). We can conclude that a very small amount of Cu^{2+} substitution not only affects the local atomic arrangement but also remarkably affects the macroscopic electrochemical redox responsiveness.

Galvanostatic charge–discharge tests were systematically performed at various current densities (C-rates) to examine the effect of Cu^{2+} substitution on the kinetics of Li^+ transport. The $LiNi_{0.5}Mn_{1.5}O_{4-\delta}$ cathode showed greater capacity fading with increasing current density compared to $LiNi_{0.49}Cu_{0.01}Mn_{1.49}O_{3.62}$ (Figure 6(a)). Even at a 5 C rate for the $LiNi_{0.49}Cu_{0.01}Mn_{1.49}O_{3.62}$ electrodes with relatively high tap density, a capacity of approximately 80% of the initial discharge capacity was maintained. The capacity dropped because the increased internal resistance was drastically improved with increasing current density by Cu^{2+} substitution. The incorporation of Cu^{2+} affects the electrochemical lithium intercalation kinetics, which are strongly associated with the bulk properties of the electrode materials (electron conductivity, Li^+ conductivity, crystal size (Li^+ internal diffusion length) etc.) and shorter diffusion length due to smaller crystal size in preference to the kinetic parameters at the electrode/electrolyte interface.

The effects of Cu^{2+} incorporation on partial density of state (PDOS) of $LiNi_{0.5}Mn_{1.5}O_{4-\delta}$ were computationally analyzed. As shown in Figure 6(b), a characteristic change in the PDOS of the Mn-3d band at the fully lithiated composition appeared near the Fermi level. Even though the smaller band gap in $LiNi_{0.5}Mn_{1.375}Cu_{0.125}O_{3.875}$ cannot be sufficiently described by the electronic conductivity, *d*-electron doping driven by the Cu^{2+} incorporation has the potential to decrease this band gap.

The effects of Cu^{2+} substitution were further investigated from the viewpoint of Li^+ conduction behaviour. Our calculation revealed the existence of four possible conduction paths with various hopping energy barrier for lithium ion transport within the spinel lattice, of which they are depending on the transition metal arrangements around the Li conduction path. The diffusion coefficient at around room temperature will be determined by the integral value of these four values since the hopping frequency will change due to thermal fluctuation (25 meV $atom^{-1}$ at 300 K). The migration paths and their corresponding energy profiles for Li^+ hopping along 8c–4a/12d–8c in $LiNi_{0.5}Mn_{1.5}O_4$ and $LiNi_{0.5}Mn_{1.375}Cu_{0.125}O_4$ are summarized in Figure 7. A low activation barrier accompanied by a symmetric profile along the 8c–4a/12d–8c route leads to preferable conduction paths for faster Li^+ diffusion in the spinel lattice. These results indicate that the migration path and the activation energy for Li^+ hopping depends heavily on the relative positions of Ni^{2+} and Cu_{Mn} as viewed from the tetrahedral Li^+ occupied sites. Lithium ions were the most efficiently conducting when Cu_{Mn} was located diagonally to Ni^{2+} sites via the Li^+ conduction pathway in our computationally predictable limited possibilities. Note that this can potentially show higher efficiency compared to stoichiometric $LiNi_{0.5}Mn_{1.5}O_4$. The minimum activation energy in all possibilities is reduced from 0.32 to 0.27 eV by Cu^{2+}

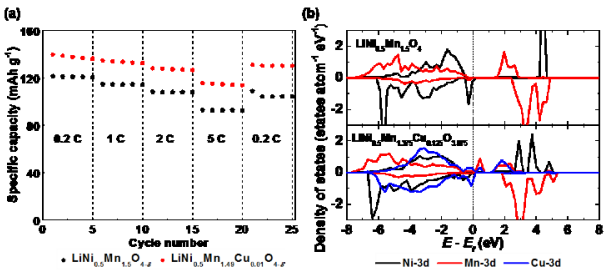

Figure 6. (a) Discharge capacities of $LiNi_{0.5}Mn_{1.5}O_{4-\delta}$/Li and $LiNi_{0.49}Cu_{0.01}Mn_{1.49}O_{3.62}$/Li cells at various C rates. (b) PDOS for Ni, Mn and Cu ions in $LiNi_{0.5}Mn_{1.5}O_4$ and $LiNi_{0.5}Mn_{1.375}Cu_{0.125}O_{3.875}$.

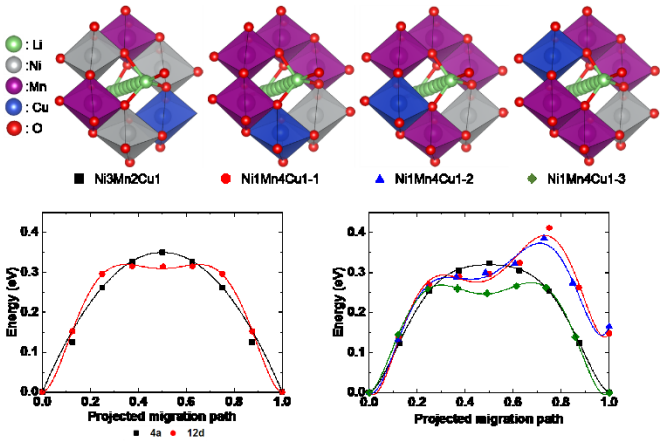

Figure 7. Migration paths along the energetically preferable 8*c*–4a/12*d*–8*c* route with different atomic arrangements and their corresponding calculated energy profiles for Li^+ hopping in the $LiNi_{0.5}Mn_{1.5}O_4$ and $LiNi_{0.5}Mn_{1.375}Cu_{0.125}O_4$ lattice.

substitution. This is equivalent to a significantly improvement of 6.6-fold increase at 300 K in terms of diffusion coefficient, as $D = a^2 v \exp(-E/k_B T)$, where a is the Li^+ hopping distance, v is the attempt frequency, E is the activation energy, k_B is Boltzmann constant, and T is temperature.

In contrast, DFT calculations determined the presence of interactions between Li^+ vacancy (V_{Li}) at the 8*c*-4*a*/12*d*-8*c* site and oxygen vacancy (V_O) at the 24*e* site, which causes significant fading in the Li^+ conduction kinetics through the interpretation for V_{Li} hopping. Since the valence state for V_{Li} is negatively charged, the activation barrier for Li^+ hopping along the 8*c*–4*a*/12*d*–8*c* path generally became larger because the Li^+ path was more positively charged. Li^+ in stoichiometric $LiNi_{0.5}Mn_{1.5}O_4$ moves in a straight line along the migration path, while Li^+ in $LiNi_{0.5}Mn_{1.375}Cu_{0.125}O_{3.875}$ with oxygen deficiency migrates tortuously at V_{Li} regardless of the local Ni^{2+}/Mn^{4+} ordering. The existence of V_O resulted in a large potential difference of >0.63 eV for Li^+ hopping to neighbouring Li^+ sites, leading to significant activation energy enhancement. These results imply that the passivation of V_O with other anions can mitigate tortuous Li^+ migration, such as F^{-1}, and are effective for deriving the C rate capability of $LiNi_{0.5}Mn_{1.375}Cu_{0.125}O_{3.875}$.

Figure 8(a) shows the discharge capacity vs. cycle number for the $LiNi_{0.5}Mn_{1.5}O_{4-\delta}$/Li cell and $LiNi_{0.49}Cu_{0.01}Mn_{1.49}O_{3.62}$ cathode/Li cell operated at 23 °C with a current corresponding to 2 C. A significant capacity loss was observed with increasing cycle number to approximately 80% of the initial capacity for the $LiNi_{0.5}Mn_{1.5}O_{4-\delta}$/Li cell after 100 cycles; the Cu^{2+}-incorporated $LiNi_{0.5}Mn_{1.5}O_{4-\delta}$/Li cells showed an obvious improvement in the cyclability with capacity retention >96%. The coulomb efficiency of the cell was almost constant at >0.95 during cycling. The absence ratio of Mn^{3+} was sufficiently retained in the $LiNi_{0.49}Cu_{0.01}Mn_{1.49}O_{3.62}$ compared to that of $LiNi_{0.5}Mn_{1.5}O_{4-\delta}$. Furthermore, retention of dark pigments was observed on the polypropylene separator after 100 cycles in the $LiNi_{0.5}Mn_{1.5}O_{4-\delta}$/Li cell, unlike that in the $LiNi_{0.49}Cu_{0.01}Mn_{1.49}O_{3.62}$/Li cells. The batteries were reusable after replacing an old separator with a new one. These results strongly suggest that Cu^{2+} substitution suppresses the dissolution of Mn ions into the electrolyte via oxidative decomposition for the liquid electrolyte at high voltages; this is widely known as a primary factor in battery performance degradation. The DFT calculation studies presented here imply that the inactivation of electrochemical redox responses for Mn^{3+}/Mn^{4+} led to significant cyclability improvement. These results strongly suggest that the incorporation of Cu^{2+} into the spinel lattice lowers the risk of capacity fading under high-voltage operation because of the occurrence of self-discharge caused by Mn metal deposition on the separator closed to the Li metal anode surface (self-discharge)[22, 23].

The possibility of significant cycle degradation during further cycles was also observed in the $LiNi_{0.49}Cu_{0.01}Mn_{1.49}O_{3.62}$ /Li cells. Characteristic redox waves were observed at 4.4 V (vs Li^+/Li) due to Cu^{2+}/Cu^{3+} redox couples diminishing and a new peak centered at 3.95 V appeared after 100 cycles (Figure 8(b)). This indicates that Mn^{3+}/Mn^{4+} redox couples will be electrochemically active after the loss of Cu^{3+} occupied at 12d sites in the spinel lattice during cycling. This could potentially promote capacity fading due to self-discharge through a disproportionation reaction. In order to mitigate the cyclability fading triggered by Cu^{3+} dissolution, we further demonstrated an ultra-thin fluoroalkylsilane SAM coating as a modifying agent[22, 23] at the $LiNi_{0.49}Cu_{0.01}Mn_{1.49}O_{3.62}$ cathode/electrolyte interface. The thickness of the FAS17-SAM coating layer was ca. 1.3 nm, as evaluated by a combination of angle-resolved XPS-Mn2p and semi-empirical analysis. As shown in Figure 8(c), the FAS17-coated half-cell showed a noticeable improvement in cyclability with capacity retention > 99% after 100 cycles with a coulomb efficiency of > 0.95. Increasing both the surface ionization potential and mitigation of direct contact with the electrolyte at the interface (through the formation of a highly-ordered FAS monolayer bound to the electrode surface) contributed to the inhibition of oxidative decomposition of the electrolyte at the cathode/electrolyte

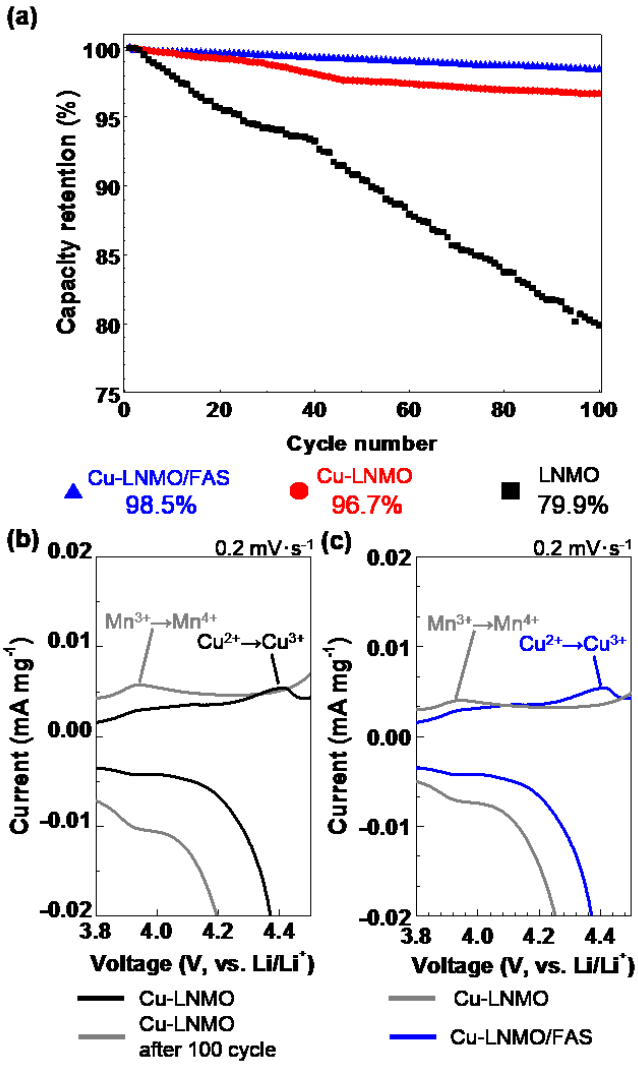

Figure 8. (a) Changes in the discharge capacity as a function of cycle number for $LiNi_{0.5}Mn_{1.5}O_{4-\delta}$/Li and $LiNi_{0.49}Cu_{0.01}Mn_{1.49}O_{3.62}$/Li cells cycled at 23 °C with a current corresponding to 2 C. (b) Changes in the cyclic voltammograms of $LiNi_{0.49}Cu_{0.01}Mn_{1.49}O_{3.62}$/Li cells after 100 cycles. (c) Effects of FAS17 coating on the changes in cyclic voltammograms of $LiNi_{0.49}Cu_{0.01}Mn_{1.49}O_{3.62}$/Li cells.

interface. We have previously reported these behaviors in $LiNi_{0.5}Mn_{1.5}O_{4-\delta}$/Li half cell and $LiNi_{0.5}Mn_{1.5}O_{4-\delta}$/C full cells, respectively[22, 23]. Furthermore, minor enhancement in the C-rate capability was further observed, which may be due to reduction of the desolvation energy for the Li^+ in the electrolyte. The FAS17-SAM can be used as insulation against Cu^{3+} dissolution at the $LiNi_{0.49}Cu_{0.01}Mn_{1.49}O_{3.62}$ electrolyte/cathode interface without affecting the power density.

Conclusions

We determined the effect of trace amounts of Cu^{2+} incorporation on the structural, electrical and electrochemical characteristics of oxygen-deficient, spinel-type $LiNi_{0.5}Mn_{1.5}O_{4-\delta}$ crystals using both experimental and computational approaches. This is the first report that provides a full picture of the local symmetry transition and cascaded macroscopic electrochemical characteristics of high-voltage spinel manganese cathodes for LIBs. These local symmetry transition-driven effects are an exciting new direction for the development of advanced cathode materials.

Conflicts of interest

There are no conflicts to declare.

Acknowledgements

This work was partially supported by JST-CREST Grant Number JPMJCR1322 JAPAN. N.Z. acknowledges JSPS KAKENHI Grant Number 17H01322. The crystal structure figures were drawn with VESTA[47].

References

1 M. Armand and J.-M. Tarascon, Building better batteries. *Nature*, 2008, **451**, 652-657.
2 M. Winter and R. J. Brodd, What Are Batteries, Fuel Cells, and Supercapacitors? *Chem. Rev.*, 2004, **104**, 4245–4270.
3 G. Q. Liu, L. Wen and Y. M. Liu, Spinel $LiNi_{0.5}Mn_{1.5}O_4$ and its derivatives as cathodes for high-voltage Li-ion batteries. *J. Solid State Electrochem.,* 2010, **14**, 2191-2202.
4 W. Zhu, D. Liu, J. Trottier, C. Gagnon, A. Guerfi, C.M. Julien, A. Mauger and K. Zaghib, Comparative studies of the phase evolution in M-doped $Li_xMn_{1.5}Ni_{0.5}O_4$ (M = Co, Al, Cu and Mg) by in-situ X-ray diffraction. *J. Power Sources*. 2014, **264**, 290-298.
5 Z. H. Xiao, Q.-Q. Cui, X.-L. Li, H.-L. Wang and Q. Zhou, Ionothermal synthesis for Mg-doped $LiNi_{0.5}Mn_{1.5}O_4$ spinel with structural stability and high-rate performance. *Ionics*. 2015, **21**, 1261-1267.
6 D. T. Murphy, S. Schmid, J. R. Hester, P. E. R. Blanchard and W. Miiller, Coordination Site Disorder in Spinel-Type $LiMnTiO_4$. *Inorg. Chem.*, 2015, **54**, 4636-4643.
7 Y.-Z. Jin, Y.-Z. Lv, Y. Xue, J. Wu, X.-G. Zhang and Z.-B. Wang, Improved electrochemical performance of $LiNi_{0.4}Ti_{0.1}Mn_{1.5}O_4$ as cathode of lithium ion battery by carbon-coating. *RSC Adv.*, 2014, **4**, 57041-57047.
8 R. Alcántara, M. Jaraba, P. Lavela, J. L. Tirado, Ph. Biensan, A. de Guibert, C. Jordy and J. P. Peres, Structural and Electrochemical Study of New $LiNi_{0.5}Ti_xMn_{1.5-x}O_4$ Spinel Oxides for 5-V Cathode Materials. *Chem. Mater.*, 2003, **15**, 2376-2382.
9 M.-C. Yang, B. Xu, J.-H. Cheng, C.-J. Pan, B.-J. Hwang and Y. S. Meng, Electronic, Structural, and Electrochemical Properties of $LiNi_xCu_yMn_{2-x-y}O_4$ ($0 < x < 0.5$, $0 < y < 0.5$) High-Voltage Spinel Materials. *Chem. Mater.*, 2011, **23**, 2832-2841.
10 M. Aklalouch, J. M. Amarilla, R. M. Pojas, I. Saadoune and J. M. Rojo, Chromium doping as a new approach to improve the cycling performance at high temperature of 5 V $LiNi_{0.5}Mn_{1.5}O_4$-based positive electrode. *J. Power Sources*, 2008, **185**, 501-511.
11 S. B. Park, W. S. Eom, W. I. Cho and H. Jang, Electrochemical properties of $LiNi_{0.5}Mn_{1.5}O_4$ cathode after Cr doping. *J. Power Sources*, 2006, **159**, 679-684.
12 W. Zhu, L. J. Trottier, C. Gagnon, A. Mauger, C. M. Julien and K. Zaghib, In-situ X-ray diffraction study of the phase evolution in undoped and Cr-doped $Li_xMn_{1.5}Ni_{0.5}O_4$ ($0.1 \leq x \leq 1.0$) 5-V cathode materials. *J. Power Sources*, 2013, **242**, 236-243.
13 X. Yang, T. Yang, S. Liang, X. Wu and H. Zhang, Modification of $LiNi_{0.5}Mn_{1.5}O_4$ high potential cathode from the inner lattice to the outer surface with Cr^{3+}-doping and Li^+-conductor coating. *J. Mater. Chem. A*, 2014, **2**, 10359-10364.
14 A. Bhaskar, W. Gruner, D. Mikhailov and H. Ehrenberg, Thermal stability of $Li_{1-\Delta}M_{0.5}Mn_{1.5}O_4$ (M = Fe, Co, Ni) cathodes in different states of delithiation Δ. *RSC Adv.*, 2013, **3,** 5909-5916.
15 J. Liu and A. Manthiram, Understanding the Improved Electrochemical Performances of Fe-Substituted 5 V Spinel Cathode $LiNi_{0.5}Mn_{1.5}O_4$. *J. Phys. Chem. C*, 2009, **113**, 15073-15079.
16 B. Ebin, S. Gürmen and G. Lindbergh, Electrochemical properties pf nanocrystalline $LiCu_xMn_{2-x}O_4$ (x = 0.2-0.6) particles prepared by ultrasonic spray pyrolysis method. *Mater. Chem. Phys.*, 2012, **136**, 424-430.
17 K. R. Chemelewski and A. Manthiram, Origin of Site Disorder and Oxygen Nonstoichiometry in $LiMn_{1.5}Ni_{0.5-x}M_xO_4$ (M = Cu and Zn) Cathodes with Divalent Dopant Ions. *J. Phys. Chem. C*, 2013, **117**, 12465-12471.
18 Z. Yang, Y. Jiang, J.-H. Kim, Y. Wu, G.-L. Li and Y.-H. Huang, Preparation of MnO_2 electrodes coated by Sb-doped SnO_2 and their effect on electrochemical performance for supercapacitor. *Electrochim. Acta*, 2014, **117**, 76-83.
19 H. Wang, T. A. Tan, P. Yang, M. O. Lai and L. Lu, High-Rate Performances of the Ru-Doped Spinel $LiNi_{0.5}Mn_{1.5}O_4$: Effects of Doping and Particle Size. *J. Phys. Chem. C*, 2011, **115**, 6102-6110.
20 H. Wang, H. Xia, M. O. Lai and L. Lu, Enhancements of rate capability and cyclic performance of spinel $LiNi_{0.5}Mn_{1.5}O_4$ by trace Ru-doping. *Electrochem. Comm.*, 2009, **11**, 1539-1542.
21 M. Mo, K.S. Hui, X. Hong, J. Guo, C. Ye, A. Li, N. Hu, Z. Huang, J. Jiang, J. Liang and H. Chen, Improved cycling and rate performance of Sm-doped $LiNi_{0.5}Mn_{1.5}O_4$ cathode materials for 5 V lithium ion batteries. *Appl. Surf. Sci.*, 2014, **290**, 412-418.
22 N. Zettsu, S. Kida, S. Uchida and K. Teshima, Sub-2 nm Thick Fluoroalkylsilane Self-Assembled Monolayer-Coated High Voltage Spinel Crystals as Promising Cathode Materials for Lithium Ion Batteries. *Sci. Rep.*, 2016, **6**, 31999 1-8.
23 D. W. Kim, S. Uchida, H. Shiiba, N. Zettsu and K. Teshima, New Insight for Surface Chemistries in Ultra-thin Self-assembled Monolayers Modified High-voltage Spinel Cathodes. *Sci. Rep.*, 2018 in press.
24 Y. Idemoto, H. Narai and N. Koura, Crystal structure and cathode performance dependence on oxygen content of

$LiNi_{0.5}Mn_{1.5}O_4$ as a cathode material for secondary lithium batteries. *J. Power Sources*, 2003, **119-121**, 125-129.

25 J.-H. Kim, S.-T. Myung, C. S. Yoon, S. G. Kang and Y.-K. Sun, Comparative Study of $LiNi_{0.5}Mn_{1.5}O_{4-\delta}$ and $LiNi_{0.5}Mn_{1.5}O_4$ Cathodes Having Two Crystallographic Structures: *Fd*-3*m* and *P*4$_3$32.*Chem. Mater.*, 2004, **16**, 906-914.

26 H. Xia, S. Tang, L. Lu, Y. Meng and G. Ceder, The influence of preparation conditions on electrochemical properties of $LiNi_{0.5}Mn_{1.5}O_4$ thin film electrodes by PLD. *Electrochim. Acta*, 2006, **52**, 2822-2828.

27 Y. Terada, K. Yasaka, F. Nishikawa, T. Konishi, M. Yoshio and I. Nakai, *In Situ* XAFS Analysis of Li(Mn, M)$_2$O$_4$ (M=Cr, Co, Ni) 5V Cathode Materials for Lithium-Ion Secondary Batteries. *J. Solid State Chem.*, 2001, **156**, 286-291.

28 K. Dokko, M. Mohamedi, N. Anzue, T. Itoh and I. Uchida, In situ Raman spectroscopic studies of $LiNi_xMn_{2-x}O_4$ thin film cathode materials for lithium ion secondary batteries. *J. Mater. Chem.*, 2002, **12**, 3688-3693.

29 T. Yang, N. Zhang, Y. Lang and K. Sun, Enhanced rate performance of carbon-coated $LiNi_{0.5}Mn_{1.5}O_4$ cathode material for lithium ion batteries. *Electrochim. Acta*, 2011, **56**, 4058-4064.

30 G. Liu, X. Kong, H. Sun and B. Wang, Long cycle life, high rate capability of truncated octahedral $LiMn_2O_4$ cathode materials synthesized by a solid-state combustion reaction for lithium ion batteries. *Ceram. Int.*, 2014, **40**, 14391-14395.

31 L. Wang, H. Li, X. Huang and E. Baudrin, A comparative study of *Fd*-3*m* and *P*4$_3$32 "$LiNi_{0.5}Mn_{1.5}O_4$". *Solid State Ionics*, 2011, **193**, 32-38.

32 S. Patoux, L. Daniel, C. Bourbon, H. Lignier, C. Pagano, F. Le Cras, S. Jouanneau and S. Martinet, High voltage spinel oxides for Li-ion batteries: From the material research to the application. *J. Power Sources*, 2009, **189**, 344-352.

33 M. Mo, K.S. Hui, X. Hong, J. Guo, C. Ye, A. Li, N. Hu, Z. Huang, J. Jiang, J. Liang and H. Chen, Improved cycling and rate performance of Sm-doped $LiNi_{0.5}Mn_{1.5}O_4$ cathode materials for 5 V lithium ion batteries. *Appl. Surf. Sci.*, 2014, **290**, 412-418.

34 W. K. Pang, N. Sharma, V. K. Peterson, J.-J. Shiu and S.-h. Wu, *In-situ* neutron diffraction study of the simultaneous structural evolution of a $LiNi_{0.5}Mn_{1.5}O_4$ cathode and a $Li_4Ti_5O_{12}$ anode in a $LiNi_{0.5}Mn_{1.5}O_4||Li_4Ti_5O_{12}$ full cell. *J. Power Sources*, 2014, **246**, 464-472.

35 G. Kresse and J. Furthmuller, Efficient iterative schemes for *ab initio* total-energy calculations using a plane-wave basis set. *Phys. Rev. B*, 1996, **54**, 11169-11186.

36 G. Kresse and J. Furthmuller, Efficiency of *ab-initio* total energy calculations for metals and semiconductors using a plane-wave basis set. *Comput. Mater. Sci.*, 1996, **6**, 15-50.

37 J. P. Perdew, A. Ruzsinszky, G. I. Csonka, O. A. Vydrov, G. E. Scuseria, L. A. Constantin, X. Zhou and K. Burke, Restoring the Density-Gradient Expansion for Exchange in Solids and Surfaces. *Phys. Rev. Lett.*, 2008, **100**, 136406.

38 P. E. Blochl, Projector augmented-wave method. *Phys. Rev. B*, 1994, **50**, 17953.

39 A. Jain, G. Hautier, S. P. Ong, C. J. Moore, C. C. Fischer, K. A. Persson and G. Ceder, Formation enthalpies by mixing GGA and GGA+*U* calculations. *Phys. Rev. B*, 2011, **84**, 045115.

40 H. Shiiba, N. Zettsu, M. Nakayama, S. Oishi and K. Teshima, Defect Formation Energy in Spinel $LiNi_{0.5}Mn_{1.5}O_{4-\delta}$ Using *Ab Initio* DFT Calculations. *J. Phys. Chem. C*, 2015, **119**, 9117-9124.

41 E. Lee and K. A. Persson, Revealing the coupled cation interactions behind the electrochemical profile of $Li_xNi_{0.5}Mn_{1.5}O_4$. *Ener. Environ. Sci.*, 2012, **5**, 6047-6051.

42 E. Lee and K. A. Persson, Solid-Solution Li Intercalation as a Function of Cation Order/Disorder in the High-Voltage $Li_xNi_{0.5}Mn_{1.5}O_4$ Spinel. *Chem. Mater.*, 2013, **25**, 2885-2889.

43 L. Wang, T. Maxisch and G. Ceder, Oxidation energies of transition metal oxides within the GGA+*U* framework. *Phys. Rev. B*, 2006, **73**, 195107.

44 S. H. Oh, K. Y. Chung, S. H. Jeon, C. S. Kim, W. I. Cho and B. W. Cho, Structural and electrochemical investigations on the $LiNi_{0.5-x}Mn_{1.5-y}M_{x+y}O_4$ (M = Cr, Al, Zr) compound for 5 V cathode material. *J. Alloy Compd.,* 2009, **469**, 244-250.

45 C. M. Julien and M. Massot, Lattice vibrations of materials for lithium rechargeable batteries I. Lithium manganese oxide spinel. *Mat. Sci. Eng. B-Solid*, 2003, **97**, 217-220.

46 M. Kunduraci and G. G. Amatucci, Synthesis and Characterization of Nanostructured 4.7 V $Li_xNi_{0.5}Mn_{1.5}O_4$ Spinels for High-Power Lithium-Ion Batteries. *J. Electrochem. Soc.,* 2006, **153**, A1345-A1352.

47 K. Momma and F. Izumi, *VESTA 3* for three-dimensional visualization of crystal, volumetric and morphology data. *J. Appl. Crystallogr.*, 2011, **44**, 1272-1276.